A molecular dynamics simulation study of crystalline 1,3,5-triamino-2,4,6-trinitrobenzene as a function of pressure and temperature

Dmitry Bedrov,[1,2,a] Oleg Borodin,[1,2] Grant D. Smith,[1] Thomas D. Sewell,[3] Dana M. Dattelbaum,[4] and Lewis L. Stevens[4]

[1]Department of Materials Science and Engineering, University of Utah, Salt Lake City, Utah 84112, USA
[2]Wasatch Molecular Inc., Salt Lake City, Utah 84108, USA
[3]Department of Chemistry, University of Missouri-Columbia, Columbia, Missouri 65211-7600, USA
[4]Dynamic and Energetic Materials Division, Los Alamos National Laboratory, Los Alamos, New Mexico 87545, USA

Quantum chemistry-based dipole polarizable and nonpolarizable force fields have been developed for 1,3,5-triamino-2,4,6-trinitrobenzene •TATB•. Molecular dynamics simulations of TATB crystals were performed for hydrostatic pressures up to 10 GPa at 300 K and for temperatures between 200 and 400 K at atmospheric pressure. The predicted heat of sublimation and room-temperature volumetric hydrostatic compression curve were found to be in good agreement with available experimental data. The hydrostatic compression curves for individual unit cell parameters were found to be in reasonable agreement with those data. The pressure- and temperature-dependent second-order isothermal elastic tensor was determined for temperatures between 200 and 400 K at normal pressure and for pressures up to 10 GPa on the 300 K isotherm. Simulations indicate considerable anisotropy in the mechanical response, with modest softening and significant stiffening of the crystal with increased temperature and pressure, respectively. For most properties the polarizable potential was found to yield better agreement with available experimental properties. © 2009 American Institute of Physics. •doi:10.1063/1.3264972•

I. INTRODUCTION

1,3,5-triamino-2,4,6-trinitrobenzene •TATB• is an energetic material used in high-performance military applications. The molecular structure of TATB, shown in Fig. 1, is characterized by strong intramolecular hydrogen bonding between neighboring amine and nitro groups. TATB exhibits remarkably low sensitivity to accidental initiation by unintended external stimuli such as shock, thermal, or electrical loading.[1,2] Numerous spectroscopic, chemical, and structural studies have been performed in attempts to understand the origin of this stability. Among the explanations that have been suggested and explored are chemical stabilization due to strong intramolecular push-pull conjugation[3] and related electronic interactions;[4] stabilization due to intermolecular hydrogen bonding;[2] centrosymmetry, or lack thereof based on second-harmonic frequency-doubling experiments;[5–8] and the low potential energy barrier to compression and glide between layers in the TATB crystal structure.[9]

Cady and Larson[10] determined that at room temperature and atmospheric pressure TATB crystallizes in a triclinic unit cell containing two molecules in the $P\bar{1}$ space group. The crystal consists of graphitic-like sheets in the a-b crystal plane, with significant inter and intramolecular hydrogen bonding in that plane •see Fig. 1•. By contrast, interplanar interactions along the c-axis are limited to weak van der Waals forces. These distinct differences in bonding along

different crystal directions lead to significant thermomechanical anisotropy, and numerous experimental and theoretical studies have been performed to characterize and explain the effects of this anisotropy on observed TATB properties. The anisotropic thermal expansion of TATB was studied by Rizzo and Kolb;[11] those workers reported an order-of-magnitude difference between the linear expansion coefficients along a and b compared to c. Olinger and Cady[12] conducted an experimental investigation of room-temperature TATB crystal structure under hydrostatic compression from normal pressure to 7.47 GPa. In order to ob-
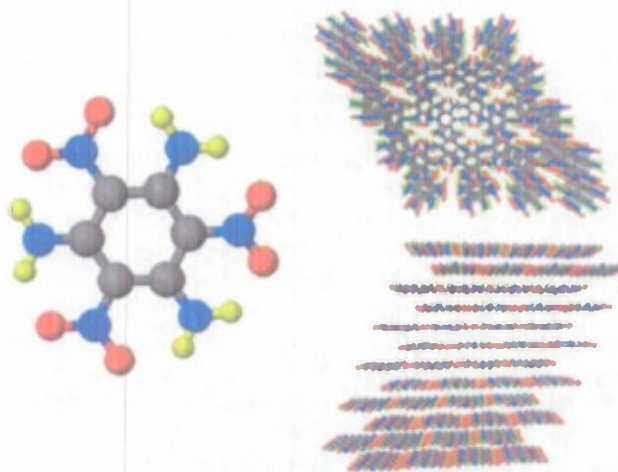

FIG. 1. Molecular and crystal structure of TATB.

tain the lattice parameters from their data, Olinger and Cady assumed that the ratio a/b was constant and also that points in adjacent a-b planes maintained fixed relative positions under compression. Recently, Stevens et al.[13] reported volumetric data for hydrostatic compression of TATB crystal for pressures up to 13 GPa. Their results were generally consistent with those of Olinger et al.,[12] although Stevens et al.[13] did report a slightly stiffer mechanical response. Interestingly, Stevens et al.[13] observed a small kink in the isotherm at P = 8 GPa when plotting the data in the pseudo shock-velocity/particle-velocity plane. Pravica and co-workers[14,15] studied the infrared spectrum of TATB under compression to 40 GPa in a diamond anvil cell using Fourier Transform Infrared Spectroscopy. They investigated shifts in spectral peaks in the far- and mid-infrared regions and observed decreases in N–H and N–O stretching frequencies with increasing pressure, indicative of increased hydrogen bonding under compression. They obtained data during both loading and unloading and found no evidence for either phase transitions or chemical decomposition in the pressure interval studied. Fits of experimental volumetric compression data to various equations of state •EOSs• have provided estimates of isothermal bulk modulus K_0 and its initial pressure derivative K'.[12,13] However, to the best of our knowledge no attempts to resolve the complete set of elastic constants for TATB crystal have been made from either experiment or theory.

Theoretical and simulation studies of TATB compression have also been reported. Pastine and Bernecker[16] reported a theoretical EOS obtained from calculations based on simple Lennard-Jones interactions that only addressed interplane interactions along the c-axis. This EOS predicted a compressibility significantly lower than values based on experiment.[13] Byrd and Rice[17] used plane wave density functional theory •DFT• calculations to investigate TATB crystal under hydrostatic compression. This work showed that DFT predictions for energetic crystals are quite sensitive to the size of basis set and that DFT provides a poor description of unit cell lattice vectors at lower pressures, presumably due to neglect of dispersion interactions in the theoretical model.

Sewell[18] reported studies of temperature-dependent unit cell volume, lattice parameters, and energies obtained from isobaric-isothermal •NPT• Monte Carlo •MC• simulations of TATB crystal, based on a simple Buckingham-plus-charges intermolecular interaction potential and extension to treat atom-centered multipoles through octupole. The effects of system size, intramolecular flexibility •fully rigid molecules versus ones that included hindered NO_2 rotations•, and order of expansion of atom-centered multipoles were considered. Although inclusion of atom-centered multipoles yielded improved fits to electrostatic potentials compared to results obtained using simple partial atomic charges, they did not lead to significantly different temperature dependencies for energy or density. By contrast, inclusion of NO_2 rotation was found to have a significant effect on both thermal expansion and specific heat.

Gee et al.[19] developed a fully atomistic flexible molecule force field •FF• and used it in molecular dynamics •MD• simulations to study pressure-volume-temperature properties of TATB crystal. In their FF Gee et al.[19] obtained Lennard-

Jones nonbonded parameters by fitting to gas-phase TATB dimer energies obtained from quantum chemistry •QC• calculations using the MP2/6-31G•d,p• theory and basis set combination for geometries relevant to the crystal. Intramolecular covalent bond and three-center angle-bending interactions were taken from the DREIDING FF while torsional potentials for NO_2 and NH_2 groups were parameterized to reproduce previously published QC calculations of the dihedral barrier heights. Gee et al.[19] reported identical values of the Lennard-Jones well depth parameters for C–C and N–N nonbonded interactions. The optimized value, 0.01 kcal/mol, is six times lower than the well depth they used for H–H interactions and is in striking disagreement with corresponding values used in other organic molecule FFs such as OPLS-AA[20] or AMBER.[21] Nevertheless, Gee et al.[19] predicted crystal structure, temperature- and pressure-dependent lattice parameters, and other structural metrics that are in good agreement with the experimental data of Olinger and Cady.[12] However, it was reported subsequently[22] that the heat of sublimation for the Gee et al.[19] FF is H_{sub} = 31.1 kcal/mol, which is significantly lower than reported experimental values due to Garza[23] •43.1 kcal/mol• and Rosen and Dickinson[24] •40.2 kcal/mol•. Taken together, these factors suggest that the Gee et al.[19] FF may significantly underestimate the interaction strength between TATB molecules in the crystal. However, another key result of the work of Gee et al.[19] is that MD predictions for TATB are highly sensitive to details of the FF employed. In particular, they showed that, starting from the experimental structure, attempts to simulate TATB crystal using generic FFs such as CVFF,[25] CFF91•950•,[26] COMPASS,[27] DREIDING,[28] and UFF •Ref. 29• resulted in phase transitions into polymorphs that are not observed experimentally. Gee et al. also reported a study using their FF in which they investigated adhesion energies between TATB crystal and various fluoropolymers.[30] In this work standard combining rules were used to obtain nonbonded interactions between TATB and the polymers. Taking into account the likely underestimation in the Gee et al.[19] TATB FF of nonbonded parameters discussed above, we believe it is difficult to have high confidence that TATB-polymer interactions would be represented accurately in those simulations.

Recently, Rai et al.[22] extended the transferable potentials for phase equilibrium •TraPPE• FF to model crystalline TATB. This FF, in our opinion, uses physically more reasonable parameters for dispersion interactions and has a significantly different distribution of atomic partial charges than the FF of Gee et al.[19] The pressure-volume-temperature behavior for TATB crystal predicted from MD simulations using this FF was in as good agreement with experimental data as that predicted using the FF model of Gee et al.[19] However, the heat of sublimation predicted from this FF is only 25.8 kcal/mol; this value is almost 40% lower than the experimental values, indicating that, despite predicting accurately the temperature and pressure dependencies of the lattice parameters, the strength of intermolecular interactions appears to be underestimated in this FF.

In the present work we report results of molecular simulations of crystalline TATB using FF models based on the

Atomistic Polarizable Potential for Liquids, Electrolytes, and Polymers (APPLE&P)[31] model. In contrast to the Gee et al.[19] and TraPPE FFs which use fixed partial atomic charges, in this work we used a polarizable FF that accounts explicitly for induced polarization effects that typically exist in condensed phase organic crystals. We show that simulations using this polarizable FF accurately predict the structure and the heat of sublimation of TATB crystal. A nonpolarizable version of the FF has also been developed; we demonstrate that it yields an adequate description of the structural and thermodynamic properties of the crystal at considerably reduced computational expense. Simulation results for pressure- and temperature-dependent properties are compared to experimental data, including newly available results for unit cell parameters that complement previously reported experimental data due to Stevens et al.[13] In addition to those FF validation results, we report complete second-order isothermal elastic tensors for a range of pressures and temperatures. To our knowledge, this is the first published report of the elastic tensor for TATB.

II. SIMULATION AND FORCE FIELD DETAILS

A. Form of the potential energy function

In this work the potential energy U^{tot} for a collection of TATB molecules is expressed as:

$$U^{tot} = U^{NB}(r) + \sum_{bonds} U^{bond}(r_{ij}) + \sum_{bends} U^{bend}(\theta_{ijk})$$
$$+ \sum_{dihedrals} U^{dihedral}(\phi_{ijkl}) + \sum_{\substack{improper \\ dihedrals}} U^{imp}(\phi^{imp}_{ijkl}), \quad (1)$$

where the sums for intramolecular terms are over all covalent bonds, bends, dihedrals, and improper dihedrals (out-of-plane bends) in the system. These individual contributions to the potential energy are described by harmonic or trigonometric functions. These forms are frequently used in MD simulations; their exact forms can be found in our previous publications.[32] The FF form is redundant in that there are more than 3N-6 covalent terms per molecule; in particular, for each TATB molecule there are terms for 24 covalent bonds, 36 bend angles, 48 dihedral angles, and 12 out-of-plane bends.

The nonbonded energy $U^{NB}(r)$ consists of the sum of two-body repulsion and dispersion terms $U^{RO}(r)$, the energy due to interactions of fixed partial atomic charges $U^{coul}(r)$, and the polarization energy $U^{pol}(r)$ arising from the interaction of induced dipoles with fixed charges and other induced dipoles,

$$U^{NB}(r) = U^{RO}(r) + U^{coul}(r) + U^{pol}(r)$$

$$= \sum_{i>j} \left\{ A_{\alpha\beta} \exp(-B_{\alpha\beta} r_{ij}) - C_{\alpha\beta} r_{ij}^{-6} \right.$$

$$\left. + D \left(\frac{12}{B_{\alpha\beta} r_{ij}} \right)^{12} \right\} + \sum_{i>j} \frac{q_i q_j}{4\pi\varepsilon_0 r_{ij}} - 0.5 \sum_i \mu_i E_i^0. \quad (2)$$

Here, the induced dipole at force center i is $\mu_i = \alpha_i E_i^{tot}$, α_i is

the isotropic atomic polarizability, E_i^{tot} is the total electrostatic field at the atomic site i due to permanent charges q_j and induced dipoles μ_j, ε_0 is the dielectric permittivity of vacuum, E_i^0 is the electric field due to fixed charges only, $A_{\alpha\beta}$ and $B_{\alpha\beta}$ are the repulsion parameters, and $C_{\alpha\beta}$ is the dispersion parameter for interaction between atoms i and j that have atom types α and β. The term $D(12/B_{\alpha\beta} r_{ij})^{12}$, with $D = 5 \times 10^{-5}$ kcal/mol for all pair interactions, is essentially zero at typical atomic separations but becomes the dominant term at $r_{ij} < 1$ Å ensuring that $U^{RO}(r)$ is repulsive at distances much smaller than the size of an atom. The Thole screening[33,34] ($a_T = 0.2$) that smears induced dipoles has been used in order to prevent a polarization catastrophe from occurring. Finally, for cross-term (heteroatom) interactions, the modified Waldman–Hagler combining rules[34,35] were used

$$A_{ij} = \sqrt{A_{ii}A_{jj}} \frac{B_{ij}^6}{B_{ii}^3 B_{jj}^3}; \quad B_{ij} = \left(\frac{2}{B_{ii}^{-6} + B_{jj}^{-6}} \right)^{1/6};$$

$$C_{ij} = \sqrt{C_{ii}C_{jj}}. \quad (3)$$

Two FFs for TATB were developed in this study: a polarizable FF with no intramolecular nonbonded interactions and a nonpolarizable model that similarly does not include any intramolecular nonbonded interactions. The necessity of excluding intramolecular nonbonded interactions is discussed below.

B. Force field parameterization

In this work we followed the same protocol that has been applied previously to FF development for a number of molecular systems[31,34] including our recent work on pentaerythritol tetranitrate (PETN).[32] Here we only briefly outline the procedure and discuss details specific to TATB. First, atomic polarizabilities are determined by fitting to the molecular polarizability of gas-phase molecules as determined from QC calculations. Second, partial atomic charges are fit to reproduce QC results for the electrostatic potential on a grid of points around a gas-phase molecule, while simultaneously providing a good description of molecular dipole and quadrupole moments (see Eq. (5) below). Third, bond lengths and equilibrium bending angles are adjusted to reproduce geometries of gas-phase molecules from QC while bending force constants are taken either from previously developed FFs or from fits to QC energies for bending-angle distortions specific to TATB. Finally, parameters for torsional and out-of-plane deformations are determined by fitting the gas-phase conformational energies obtained from QC calculations for selected distortions in TATB.

Atomic polarizabilities. Calculations of gas-phase atomic polarizabilities for TATB, performed at the M052X/aug-cc-pvDz level of theory and basis set,[36] indicate very large anisotropy; specifically, the molecular polarizability in the direction perpendicular to the molecular plane is about a factor of three smaller than the in-plane polarizability ($\alpha_\perp = 10.9$ Å^3, $\alpha_\parallel = 30.6$ Å^3). However, in the FF form used here, molecular polarizability is determined as a sum of iso-

TABLE I. Force field parameters.

Atom type	Atomic polarizability $\cdot \cdot \text{Å}^3 \cdot$	Atomic charge $q \cdot e \cdot$	A $\cdot kcal\, mol^{-1} \cdot$	B $\cdot \text{Å}^{-1} \cdot$	C $\cdot kcal\, \text{Å}^6\, mol^{-1} \cdot$
$C \cdot \cdot NO_2 \cdot$	0.70	0.2839	107 023.9	3.640S	SS4.01
$C \cdot \cdot NH_2 \cdot$	0.70	• 0.202S	107 023.9	3.640S	SS4.01
$N \cdots O_2 \cdot$	1.0	0.S66S	13 783.9	3.3333	423.36
$N \cdots H_2 \cdot$	1.0	• 0.S77S	39 091.8	3.31S8	833.48
O	1.0	• 0.42S2	15 923.10	3.6446	239.07
H	0.21	0.3900	7584.2	5.2846	8.23

Bond type	Bond length •constrained, Å•	Bend type $U_B = 0.SK_B \cdots \cdot_0 \cdot^2$	K_B •kcal mol^{-1} rad^2•	$\cdot_0$ •deg•
C–C	1.440	$C–C \cdot NH_2 \cdot –C$	144	118.4
$C–N \cdot O_2 \cdot$	1.427	$C–C \cdot NO_2 \cdot –C$	144	121.6
$C–N \cdot H_2 \cdot$	1.322	$C–C–N \cdot H_2 \cdot$	140	121.7
N–O	1.230	$C–C–N \cdot O_2 \cdot$	140	119.2
N–H	1.010	C–N–O	140	116.8
		C–N–H	110	112.0
		O–N–O	9S	117.3
		H–N–H	12S	119.0

Torsion type $U_T = \cdot 0.SK_{T,i} \cdot 1 \cdot \cos \cdot i \cdot \cdots$	$K_{T,1}$ •kcal mol^{-1}•	$K_{T,2}$ •kcal mol^{-1}•	Improper dihedral type $U_{ID} = 0.SK_{ID} \cdot^2$	K_{ID} •kcal mol^{-1} rad^2•
C–C–C–C	0.0	S.3S	$C–C–C–N \cdot$	36.S
C–C–C–N	0.0	20.0	$O–N–O–C \cdot$	89.3
N–C–C–N	0.0	20.0	$H–N–H–C \cdot$	2.1
H–N–C–C	0.0	8.88		
O–N–C–C	0.0	1.60		

tropic atomic polarizabilities, which leads to isotropic over-allmolecular polarizability because intramolecular induced-dipole/induced-dipole interactions are neglected. The latter choice was made in order to improve the description of the electrostatic potential around a molecule •as described below•. Thus, while we can match the scalar value, averaged over all directions, of molecular polarizability obtained from QC it is impossible within our approach to capture the anisotropy of the molecular polarizability. In previous works we assigned atomic polarizabilities such that the average molecular polarizability is equal to that obtained from QC calculations. Initially, we followed the same procedure for TATB; some atomic polarizabilities were adopted from previously developed FF for alkanes and ethers while others were adjusted to match the average molecular polarizability $\bar{\cdot} = 23.6$ Å^3. We subsequently determined that at high pressures simulations using these polarizabilities resulted in poor convergence of the iterative procedure used for determination of induced dipole moments. We think this was due to significant overestimation of the molecular polarizability in the direction perpendicular to the molecular plane that resulted from the use of the average molecular polarizability in those simulations. This perpendicular direction corresponds to the stacking motif in TATB crystal •Fig. 1• and is the one that undergoes the largest changes under compression. Therefore, the atomic polarizabilities for carbon and nitrogen were reduced empirically to facilitate reliable convergence of induced dipoles at higher pressure as well as provide a better

agreement of molecular polarizability with that predicted from QC calculations for the perpendicular direction. •Even so, the results discussed in Sec. III below suggest that treatment of induced polarization requires additional adjustment for simulations at pressures in excess of 6 GPa.• The final atomic polarizabilities are given in Table I; they result in an isotropic molecular polarizability of $\bar{\cdot} = 17.46$ Å^3.

Partial atomic charges. In order to establish partial atomic charges, the electrostatic potential was calculated at the MP2/aug-cc-pvDz//M052X/aug-cc-pvDz level for a Cartesian grid of • 10^5 evenly spaced points surrounding the low-energy gas-phase conformer of TATB. The molecular dipole •$_i$ and quadrupole • $_i$ moments were calculated using the same combinations of theory and basis set. Charge bond increments were used to calculate partial atomic charges. The value of the partial charge q_i positioned on atom i is calculated as a sum of all charge bond increments that involve atom i as shown in Eq. •4•.

$$q_i = \sum_{j}^{nBonds} \cdot_{ij} \cdot \qquad \cdot 4 \cdot$$

A set of charge bond increments •$\cdot$• was determined by minimizing the objective function

$$\chi^2 = \sum_{j=1}^{N_{grid}} \frac{1}{N_{grid}} \left(\phi_j^{OC} - \phi_j^{FF} \right)^2 + \ldots \left(\mu^{OC} - \mu^{FF} \right)^2$$

$$+ \ldots \left(Q^{OC} - Q^{FF} \right)^2 \qquad \qquad •5•$$

where ϕ_j^{OC} and ϕ_j^{FF} are the electrostatic potential at the jth grid point from QC and the trial FF, μ^{OC} and μ^{FF} are molecular dipole moments, and Q^{OC} and Q^{FF} are quadrupole moments from QC and the FF, respectively. The relative weights $\ldots$ for fitting the electrostatic potential, dipole moments, and quadrupole moments, respectively, were set to 1.0, 0.1, and 0.05. Electrostatic potential grid points closer than 1.8 Å to oxygen, 1.5 Å to hydrogen, 2.5 Å to carbon, and 2.2 Å to nitrogen atoms were excluded from the fit, as were points further than 4.0 Å from the nearest atom.

In FFs for molecular systems the van der Waals and electrostatic interactions are typically excluded for closely bonded atoms •separated by one or two bonds, the so-called 1–2 and 1–3 interactions•. For atoms separated by three bonds •1–4 interactions• these interactions are either included fully or scaled by some factor depending on the FF or •in some cases• chemical details of the system. For nonpolarizable FFs the fitting of partial atomic charges using the procedure described above is independent of the details of exclusion of intramolecular interactions since those interactions do not influence the electrostatic field around the molecule. However, for polarizable FFs the details of intramolecular interactions become important since dipole moments induced on each atom, which are determined by both inter- and intramolecular interactions, do influence the electrostatic field at a given grid point. Initially, we attempted to fit the partial atomic charges while allowing for intramolecular interactions between atoms separated by three or more bonds. However, we found that the objective function in Eq. •5• was uncharacteristically large $\langle \chi^2 \rangle = 1.8$ kcal/mol per grid point•, indicating a relatively poor description of the electrostatic potential around the molecule. As can be seen from the molecular structure •Fig. 1•, TATB has several atomic pairs that are separated by more than three bonds yet have quite small interatomic separations. In this case it is difficult to define a simple bond-based exclusion list for intramolecular interactions that would provide a reasonably charge-neutral interaction between individual atoms and the remaining parts of the molecule. For example, if we select any nitrogen atom and apply standard exclusion of 1–2 and 1–3 terms then its interaction with carbon atoms of neighboring amine •or nitro• groups will be excluded while interactions with nitrogen, hydrogen •or oxygen• atoms that are further removed in terms of connectivity yet are in very close proximity spatially will be included. We believe that this leads to an incorrect distribution of induced atomic polarization that in turn results in a poor description of the electrostatic potential. The more appropriate way to exclude/include intramolecular interactions would be to use a group-based approach where each group is defined such that its total charge is approximately zero. However, while doable, implementation of such

an approach is rather complicated taking into account the molecular structure of TATB. Therefore, we have decided to exclude all intramolecular interactions •van der Waals and electrostatic• in our FF model. In this case, no dipole moments are induced due to intramolecular interactions and hence description of the electrostatic potential around a molecule depends only on the arrangement of fixed partial atomic charges. Charge fitting with this approach yielded a much-improved description of the electrostatic potential $\langle \chi^2 \rangle = 0.88$ kcal/mol per grid point•. The resulting partial atomic charges obtained from the fit of bond increments based on this procedure are given in Table I.

Repulsion-dispersion parameters. The C–C repulsion and dispersion parameters were fit to the experimental density and ΔH_{vap} of benzene, those for $N \cdot H_2 \cdot - N \cdot H_2 \cdot$ and H–H were fit to to the experimental densities and heats of vaporization for hydrazine and methyl hydrazine, those for O–O were taken from the previous work on PETN,[32] and those for $N \cdot O_2 \cdot - N \cdot O_2 \cdot$ were adjusted to optimize the description of TATB unit cell parameters and ΔH_{sub}. In Ref. 37 we provide a table containing density and ΔH_{vap} obtained using these repulsion-dispersion parameters for benzene, hydrazine, and methyl hydrazine.

The nitrogen atoms in amine groups and nitro groups were treated separately. Due to the relatively large withdrawal of electron density from the nitro group nitrogen atom by the bonded oxygen atoms, that nitrogen has a relatively large positive charge; thus, it is reasonable to expect that it will have effectively smaller van der Waals interactions compared to the amine nitrogen. All repulsion and dispersion parameters are given in Table I.

Valence bonds and bends. Bond lengths were set to the average values of those in an isolated TATB molecule as predicted at the M052X/aug-cc-pvDz level. In our previous simulations[32] of PETN crystals we showed that for hydrostatic compressions of up to 9 GPa •the highest pressure investigated in that study• constraining the covalent bond lengths had little effect on the predicted properties of the crystal. Since using fixed covalent bond lengths allows use of a considerably larger time step compared to simulations with flexible bonds, in the present work we chose to use fixed covalent bond lengths; consequently, bond stretching force constants were not parameterized. Equilibrium bending angles θ_0 were fit to reproduce the equilibrium geometry of TATB predicted at M052X/aug-cc-pvDz level. The mean-square deviation of TATB bending angles obtained from molecular mechanics calculations with the FF from the corresponding QC values was 0.30°. Most of the bending force constants were transferred from previous FFs[31,32] without change; exceptions are parameters for the NH_2 group, which were fit to reproduce MP2/aug-cc-pvDz//M052X/aug-cc-pvDz energies for amine group bending and out-of-plane deformation. Equilibrium bond lengths, bending angles and three-center angle-bending force constants are given in Table I.

Out-of-plane deformation potentials. The H–N–H–C* out-of-plane deformation was adjusted to reproduce QC calculations at the MP2/aug-cc-pvDz//M05-2X/aug-cc-pvDz level for distortion of the out-of-plane angle given here as
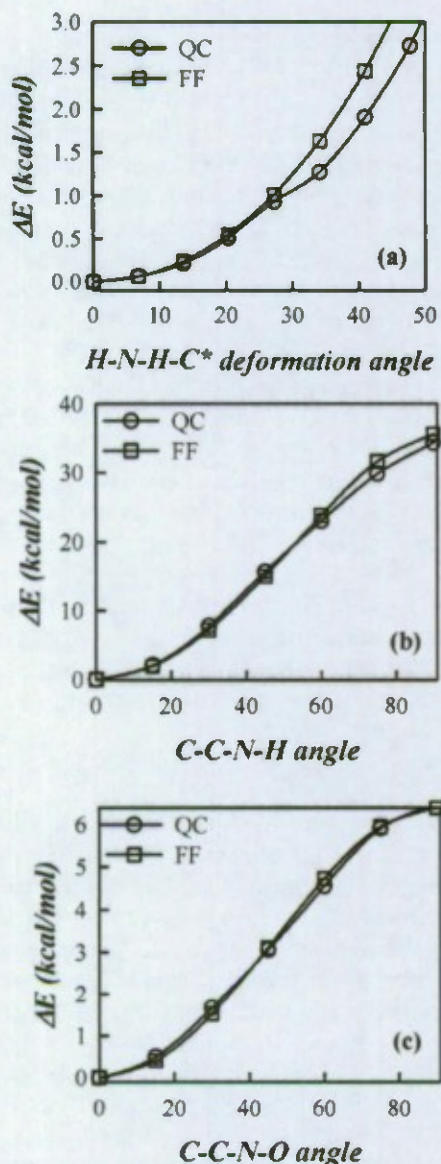
FIG. 2. Relative energies for •a• the deformation energy for H–N–H–C* out-of-plane bending, •b• the • NH_2 group rotation, and •c• the • NO_2 group rotation as obtained from molecular mechanics •MM• calculations using the FF developed in the present study and QC calculations at the MP2/aug-cc-pvDz//M05-2X/aug-cc-pvDz level. In both QC and MM calculations the • NH_2 and • NO_2 groups have been constrained to planar geometry.

the angle between the C–N bond and the NH_2 plane. The comparison between QC data and FF prediction for potential energy as a function of the out-of-plane angle is shown in Fig. 2•a•. The out-of-plane bending potential for the O–N–O–C* was taken to be the same as for the O–N–O–N* from our previous work on DMNA.[38] Force constants for all out-of-plane deformations used in this work are given in Table I.

Dihedral potentials. Dihedral potentials were determined by fitting to the relative energies for independent rotations about the C–C–N–O and C–C–N–H dihedrals in TATB obtained from QC calculations at the MP2/aug-cc-pvDz//M05-2X/aug-cc-pvDz level. The resulting dihedral parameters are

given in Table I. A comparison between QC and FF predictions for the conformational energies and geometries for these moieties is provided in Figs. 2•b• and 2•c•.

C. Simulation protocol

Our simulations of TATB crystals were performed using the molecular simulation package LUCRETIUS,[39] which has the capability to handle induced polarization effects. The systems studied contained 192 TATB molecules corresponding to 96 unit cells •a 4• 4• 6 supercell•. Periodic boundary conditions were used in all simulations. Covalent bond lengths were constrained using the velocity-Verlet form of the SHAKE algorithm.[40] The Ewald summation method was used for treatment of long-range electrostatic forces between partial charges and between partial charges and induced dipoles •k = 7^3 reciprocal vectors and • = 0.23 were used•. A tapering function

$$f•x• = 1 + \frac{2x^3 • 3• Rx^2}{• R^3} \qquad •6•$$

was used to drive the induced-dipole/induced-dipole interactions to zero over a separation interval • R = R_c • R_{taper} where R_c is a cutoff set to 11 Å; R_{taper} = 10 Å is the distance at which the scaling begins; and x = R • R_{taper}, where R is the dipole-dipole separation for R_{taper}• R• R_c. This function is equal to unity •i.e., no scaling• at R_{taper} and smoothly approaches zero •i.e., complete screening• at R_c. The derivative of this function also approaches zero at R_c, therefore ensuring that there are no force discontinuities at the cutoff radius. Induced dipoles were calculated via a direct iteration with a predictor-corrector method. A cutoff of 11 Å was used for all van der Waals interactions and the real part of electrostatic interactions in the Ewald summation.

The simulations were performed using the combined MD-MC approach used in our previous simulations of crystals of energetic materials.[32,41] Specifically, a 500 fs trajectory segment of isochoric-isothermal MD •NVT-MD• was followed by 20 attempted changes in the volume and shape of the simulation cell based on NPT rigid molecule MC •NPT-MC•. The final configuration from the kth NPT-MC sequence and final velocities from the kth NVT-MD segment defined the initial point in phase space for k + 1st NVT-MD/NPT-MC segment. For NVT-MD segments a multi-timestep reversible reference system propagator algorithm[42] was employed; a time step of 0.5 fs was used for bonding, bending, dihedral, and out-of-plane deformation motions, while a 1.0 fs timestep was used for all nonbonded interactions. Starting with a configuration corresponding to the experimental structure at room temperature and P = 0 GPa, equilibration runs of length 200 ps •8000 NPT-MC samples• were performed for each thermodynamic state considered. The initial phase space point for equilibration at successively higher pressures was taken from the equilibration run at the next lower pressure once it had reached steady-fluctuating values of the lattice parameters; a similar approach was used for successive changes in temperature at atmospheric pressure. The MC step size for a given thermodynamic state was adjusted during the first 100 ps of equilibration to yield

TABLE II. Unit cell parameters and volume and heat of sublimation obtained from MD-MC simulations and experiments at 300 K and atmospheric pressure.

	Experiment	Simulation, polarizable FF	Deviation •%•	Simulation, nonpolarizable FF, •polarizable FF charges scaled by 1.20•	Deviation •%•
a •Å•	9.010[a]	8.946	• 0.71	8.984	• 0.29
b •Å•	9.028[a]	8.974	• 0.60	9.022	• 0.07
c •Å•	6.812[a]	6.8S2	0.S9	6.86S	0.78
• •deg•	108.S8[a]	107.48	• 1.01	107.67	• 0.84
• •deg•	91.82[a]	91.6S	• 0.18	90.93	• 0.97
• •deg•	119.97[e]	120.03	0.0S	120.01	0.03
V •Å³•	442.S2[a]	443.4S	0.21	449.46	1.S6
• H_{sub} •kcal/mol•	43.1[b]	40.4	• 6.S	41.6	• 3.7
	40.2[c]		0.S		3.S

[a]From Ref. 10.
[b]From Ref. 23.
[c]From Ref. 24.

• 40%–50% acceptance probability, after which it was held constant for the duration of equilibration and production simulation for that state. Production runs consisted of 1.0 ns NVT-MD •40 000 NPT-MC observations• for each thermodynamic state considered.[43]

To verify that the results of our NVT-MD/NPT-MC simulations are insensitive to particular choices of simulation protocol parameters we conducted four case studies for one of the systems. Specifically, for a nonpolarizable model with charges increased by 20% relative to values used in the polarizable FF •see Sec. III A•, simulations at 300 K and atmospheric pressure were performed using the following combinations of simulation parameters: •a• 500 fs NVT-MD, 20 NPT-MC attempts with • h=0.05 Å •i.e., the original scheme described above; here and below, • h is the maximum allowed change in any of the six nonzero elements of the 3• 3 upper triangular matrix that specifies the dimensions of the simulation cell•; •b• 500 fs NVT-MD, 20 NPT-MC attempts, • h=0.1 Å; •c• 2000 fs NVT-MD, 80 NPT-MC attempts, • h=0.05 Å; and •d• 2000 fs NVT-MD, 20 NPT-MC attempts, • h=0.05 Å. By increasing • h from 0.05 Å •case a• to 0.1 Å •case b• the probability of accepting a MC shape/volume change decreased from • 48 to • 23%. In cases c and d, we increased the length of MD segments from 500 fs to 2 ps and either increased the number of MC attempts to 80 •thereby maintaining the original relative ratio of MD time steps to MC trial moves, case c•, or kept the number of attempted MC volume changes fixed at 20 but increased the total length of NVT-MD to 4 ns •case d•. In each case considered, 40 000 MC volume changes were attempted and used to form the elastic tensor. In Ref. 37 we report the resulting elastic stiffness coefficients, as well as bulk and shear moduli, obtained for each of these four case studies. Since the mechanical properties are defined in terms of fluctuations in volume and shape of the simulation cell they are quite sensitive to the distributions of microscopic strain •compared to simple first moments used to obtain, for example, the lattice parameters or simulation cell volume•. Table S2 shows that for the four cases studied 19 of the 21 elements of the stiffness tensor overlap to within two standard deviations of the mean, while for the isotropic moduli three out of four properties yield agreement to within two standard deviations of the mean.

Gas-phase simulations were conducted using a Brownian dynamics integrator for an ensemble of TATB molecules with intermolecular interactions turned off •i.e., an ideal gas•. Results of these simulations were used to calculate the heat of sublimation.

III. RESULTS AND DISCUSSION

A. TATB unit cell parameters at ambient conditions

Average unit cell parameters obtained for TATB at atmospheric pressure and 300 K using the polarizable FF are reported in Table II, where we also provide experimental values obtained by Cady and Larson.[10] Deviations for the a, b, and c unit cell parameters are less than 1%, which is comparable to the accuracy of simulations using Gee et al.[19] and TraPPE •Ref. 22• nonpolarizable FFs. Predicted unit cell angles, • in particular, are in good agreement with experiment and are somewhat better than those predicted from previous simulations. The resulting average volume of the unit cell is about 0.2% larger than experimental value. Table II also contains a comparison of the heat of sublimation • H_{sub} obtained from our simulations to the two experimental values. Unlike predictions from simulations using the FFs of Gee et al.[19] and the TraPPE, both of which underestimated • H_{sub} by 30%–40%, our value agrees with experiment to within a few percent suggesting that our FF provides a more accurate description of the strength of intermolecular interactions of TATB molecules in the crystal.

To investigate the importance of inclusion of induced polarization in our simulations we also conducted simulations in which atomic polarizabilities of all atoms were set to zero. Since all intramolecular interactions were excluded in our parameterization of partial atomic charges, setting atomic polarizabilities to zero does not influence the description of the electrostatic potential around a single TATB molecule in the gas phase. All other FF parameters were kept exactly the same as in polarizable version of FF. Our simulations using this nonpolarizable FF predicted cell dimensions that are off

by +0.54, +0.73, and +0.57% from experiments for a, b, and c, respectively. Unit cell angles were 106.7°, 92.1°, and 120.0°, and the unit cell volume was 456.82, which is 3.2% greater than the experimental value of Cady and Larson. The heat of sublimation obtained from simulations using this nonpolarizable FF was 35.9 kcal/mol, which is significantly lower than the experimental value.

In principle, one can make empirical adjustments to the FF to improve prediction from simulations using the nonpolarizable FF. In previous work[38] such empirical adjustment was implemented by uniform rescaling of partial atomic charges, resulting in an increase in the molecular dipole moment and therefore effectively compensating for the missing •in nonpolarizable FF• induced polarization effects in the condensed phase. Note that this scaling comes at the expense of a serious degradation in the description of the electrostatic potential around a single gas-phase TATB molecule as well as the gas-phase dipole and quadrupole moments. We have tried a similar approach for TATB crystal, increasing the partial atomic charges by as much as 30%. We found that simulations using the nonpolarizable FF with partial charges increased by 20% showed the best •among nonpolarizable simulations with various uniform charge scalings• agreement with experiment as illustrated in Table II. As one can see from the table, simulations with charges increased by 20% yield good reproduction of • H_{sub} but still overestimate the unit cell volume by 1.6%. Further increase in partial atomic charges did not improve the description of the unit cell volume but continued to increase the calculated • H_{sub}. Therefore, it appears that improving prediction of both density and heat of sublimation for the nonpolarizable FF is challenging. This further illustrates that inclusion of induced polarization is important for capturing all important interactions in TATB crystal, which should lead in turn to more accurate description of structural and thermodynamic properties of this material.

B. Pressure dependence of TATB unit cell parameters

MD-MC simulations of the TATB crystal were conducted using polarizable and nonpolarizable •with 20% scaled charges• FFs for pressures up to 10 GPa. In Fig. 3 we show the pressure dependence of unit cell dimensions. Results obtained from simulations using both polarizable and nonpolarizable FFs are compared to experimental data of Olinger and Cady[12] and Stevens et al.[13] The latter are based upon additional analysis by the authors of Ref. 13 that did not appear in their original publication. For convenience, these data are also shown in tabular form in Table III. Figure 3 reveals that despite scatter in experimental data there is some systematic difference in pressure dependence of unit cell dimensions from the two experimental data sets. Taking into account this discrepancy between experimental data, predictions from simulations using both FFs are consistent with experiment. We note that the pressure dependence of the a, b, and c unit cell parameters obtained from simulations using the nonpolarizable FF is basically the same as obtained from the polarizable FF.

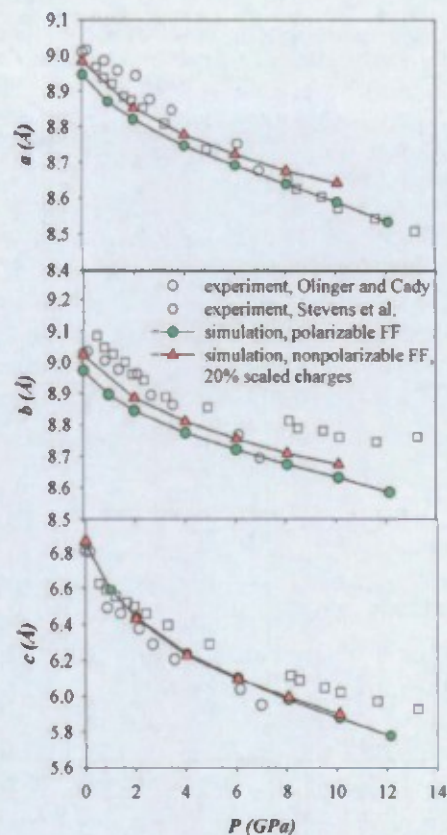Figure 4 compares the dependence of unit cell angles on

FIG. 3. Unit cell dimensions as a function of pressure as obtained from MD-MC simulations and two experiments.

pressure as obtained from simulation and experiments. Note that the two sets of experimental results exhibit noticeable differences; in particular, the measurements of Stevens et al.[13] show noticeably larger pressure dependence for • and • angles than in the older measurements. Simulation results are in good agreement with experiment for the angles • and • but systematically underestimate •. Finally, in Fig. 5 unit cell volume is shown as function of pressure. Excellent agreement between both simulation results and both sets of experimental data is obtained over entire interval of pressures investigated.

C. Temperature dependence of TATB unit cell parameters

Simulations in the temperature range between 200 and 400 K at atmospheric pressure showed almost linear dependence of unit cell dimensions on temperature. Simulations with both the polarizable and nonpolarizable •20% scaled charges• FFs showed that thermal expansion in the direction perpendicular to TATB layers stacking •along c axis• is almost an order of magnitude larger than for two other directions. For both FFs simulations predicted linear thermal expansion of 1• 10^{-4}, 1• 10^{-4} and 9• 10^{-4} Å/K for a, b, and c unit cell dimensions, respectively. These thermal expansion coefficients are very similar to those obtained from previous simulations using Gee et al.[19] and TraPPE •Ref. 22• FFs. Comparison with experimental values for linear thermal expansion coefficients[12] •• 1• 10^{-4}, 2• 10^{-4}, and 1.7

TABLE III. Unit cell dimensions extracted from experiments of Stevens et al., Ref. 13.

Pressure •GPa•	a •Å•	b •Å•	c •Å•	• •deg•	• •deg•	• •deg•
0.5600	8.9671	9.0821	6.6242	110.6190	93.0440	118.9250
0.8500	8.9372	9.0472	6.5919	110.4758	93.2130	118.9100
1.2000	8.9201	9.0250	6.5571	110.4850	93.2510	118.9660
1.6600	8.8846	9.0001	6.5199	110.6200	93.4120	118.8670
1.9500	8.8749	8.9609	6.4976	110.7200	93.3560	119.1630
2.4200	8.8525	8.9424	6.4607	110.8767	93.5040	118.9640
3.2900	8.8087	8.8885	6.3963	111.0133	93.6910	119.0320
4.9500	8.7373	8.8547	6.2898	111.3570	94.2640	118.4730
8.1800	8.6510	8.8133	6.1145	112.5060	95.5259	117.5540
8.5300	8.6247	8.7889	6.0885	112.4983	95.5370	117.6220
9.5300	8.6027	8.7814	6.0461	112.8150	95.8440	117.3280
10.1700	8.5716	8.7608	6.0225	112.9080	96.2880	116.9200
11.6400	8.5433	8.7458	5.9713	113.4380	96.5210	116.8300
13.2200	8.5073	8.7629	5.9309	114.2140	96.5930	116.6340

• 10^{-3} Å/K for a, b, and c parameters, respectively• shows that while for the a dimension simulations somewhat overestimate the thermal expansion coefficient, the opposite trend is observed for the b and c directions. Similarly, simulations •both FFs• yield a volumetric thermal expansion coefficient of 0.07 $Å^3$/K which is smaller than the experimental value of 0.14 $Å^3$/K. It is interesting to point out that independently of which FF is used •Gee et al.;[19] TraPPE; this work, polarizable, or nonpolarizable with increased charges•, the predicted thermal expansion coefficients are very similar, indicating a surprising insensitivity of thermal expansion to the details of FF parameters.

D. TATB elastic coefficients

Complete isothermal second-order elastic tensors and derived isotropic bulk and shear moduli •K and G, respectively• were determined for TATB by applying the Parrinello–Rahman strain-strain fluctuation formula[44] to our simulation data. Results for both FF models •polarizable and nonpolarizable with scaled charges• were obtained for six evenly spaced pressures between 0 and 10 GPa on the 300 K isotherm and for five evenly spaced temperatures between 200 and 400 K at atmospheric pressure. In the Parrinello–

Rahman approach the elastic compliance tensor S_{ij} is constructed from observations of simulation cell size and shape obtained from an NPT simulation; the elastic stiffness tensor C_{ij} is simply the matrix inverse of the compliance tensor. Details of our implementation of the approach have been published previously.[41] In the triclinic TATB crystal all 21 unique elements of the elastic tensor are, in general, nonzero, and are reported here. To the best of our knowledge there are no previous predictions or measurements available for comparison, with the exception of bulk modulus values based on EOS fits to isothermal compression data.

Results for 300 K and 1 atm. Results for the isothermal elastic stiffness tensor obtained at 300 K and atmospheric pressure are reported in Table IV. Results for the polarizable and nonpolarizable FFs are comparable, as is shown graphically for the stiffness tensor in Fig. 6. The most obvious difference seen there is that C_{11} and C_{22} for the two FFs differ by more than one estimated standard deviation of the mean •1• •, with larger values obtained for the polarizable FF. •In fact, eight of the nine "orthotropic" elements of the stiffness tensor are larger for the polarizable FF than for the nonpolarizable one, but five of the nine pairs overlap within 1•, and all but C_{11} and C_{22} overlap within 2• .• The hydrostatic compression and thermal expansion of TATB are
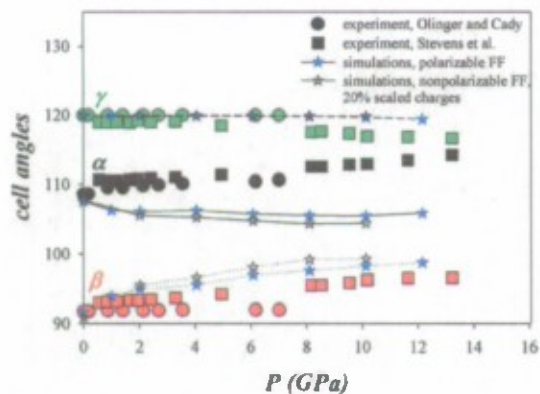

FIG. 4. Unit cell angles as a function of pressure as obtained from MO-MC simulations and two experiments.
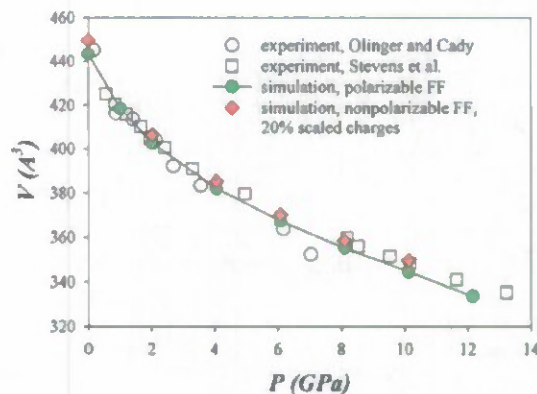

FIG. 5. Unit cell volume as a function of pressure as obtained from MD-MC simulations and two experiments.

TABLE IV. Elastic stiffness coefficients and derived isotropic moduli calculated at $T = 300$ K, $P = 0$ GPa. •Units are GPa.•

	Polarizable FF	Nonpolarizable FF		Polarizable FF	Nonpolarizable FF
C_{11}	65.7 ± 0.5[a]	57.7 ± 0.5	C_{16}	1.0 ± 1.0	0.0 ± 1.0
C_{22}	62.0 ± 1.0	58.0 ± 1.0	C_{24}	0.6 ± 0.2	0.6 ± 0.2
C_{33}	18.3 ± 0.5	17.0 ± 0.5	C_{25}	−0.5 ± 0.2	−0.5 ± 0.3
C_{44}	1.4 ± 0.3	1.0 ± 0.3	C_{26}	1.0 ± 1.0	2.0 ± 0.8
C_{55}	0.68 ± 0.06	0.6 ± 0.2	C_{34}	0.2 ± 0.3	−0.1 ± 0.4
C_{66}	21.6 ± 0.7	20.3 ± 0.8	C_{35}	−0.4 ± 0.1	−0.3 ± 0.2
C_{12}	18.5 ± 0.5	16.2 ± 0.7	C_{36}	−0.4 ± 0.7	−1.0 ± 0.5
C_{13}	4.0 ± 2.0	3.2 ± 0.5	C_{45}	0.1 ± 0.2	0.01 ± 0.04
C_{23}	5.0 ± 1.0	5.7 ± 0.6	C_{46}	0.3 ± 0.2	−0.5 ± 0.1
C_{14}	−0.2 ± 0.3	0.1 ± 0.1	C_{56}	0.4 ± 0.1	0.1 ± 0.1
C_{15}	−1.0 ± 0.1	−0.9 ± 0.2			
K_{Reuss}[b]	14.0 ± 1.0	13.2 ± 0.5			
G_{Reuss}[b]	2.0 ± 0.2	1.8 ± 0.1			
K_{Voigt}[c]	22.3 ± 0.3	20.3 ± 0.2			
G_{Voigt}[c]	12.6 ± 0.2	11.5 ± 0.2			

[a]Reported values were obtained from the overall 1 ns simulation •40 000 MC observations•. Uncertainties correspond to one standard deviation of the mean obtained from four contiguous 250 ps •10 000 MC observation• subsamples.
[b]Obtained from the compliance tensor •see Ref. 37•. Uncertainties were obtained by application of standard error propagation methods.
[c]Obtained from the stiffness tensor. Uncertainties were obtained by application of standard error propagation methods.

highly anisotropic and this is clearly reflected in the individual elastic tensor elements. For example, for the polarizable FF we predict values $C_{11} = 65.7$ GPa, $C_{22} = 62$ GPa, and $C_{33} = 18.3$ GPa. These elastic coefficients correspond nominally to deformations along the a, b, and c crystal axes, respectively, and are consistent with the TATB crystal packing motif in which layers of essentially planar molecules, held together by hydrogen-bonds in the a-b plane, stack into layers along the c axis that are held together by weak dispersion interactions. Similar remarks apply to the shear elastic coefficients, $C_{44} = 1.4$ GPa, $C_{55} = 0.68$ GPa, and $C_{66} = 21.6$ GPa •polarizable FF• corresponding roughly to deformations of lattice angles •, •, and •, respectively. The angle
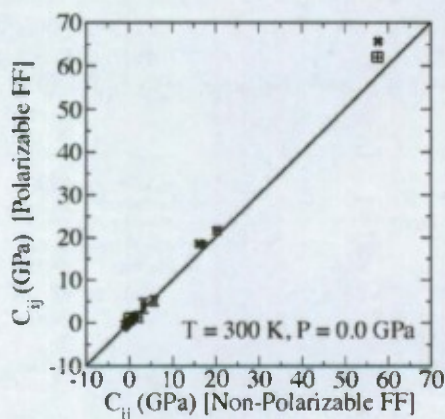

FIG. 6. Comparison between elastic stiffness tensor elements for TATB crystal computed at •$T = 300$ K, $P = 0$ GPa• using the polarizable •ordinate• and nonpolarizable •abscissa• FF models. Uncertainties represent one estimated standard deviation of the mean. The diagonal line is included as a guide for the eyes; points falling on the line correspond to equal values for both FF models.

• is defined by the a and b crystal axes; the energy required to impose a shear strain in the hydrogen-bonded plane that contains them is much larger than those required to impose shear strains in the planes whose definitions involve the c-axis. Hence, one would expect C_{66}• •C_{44}, C_{55}• in agreement with the calculated result. Analogous considerations can be used to explain the relative magnitudes for the dilational coefficients, C_{12}• •C_{13}, C_{23}•.

Isotropic bulk and shear moduli were calculated using standard expressions for the Voigt and Reuss bounds, corresponding to conditions of uniform strain and uniform stress, respectively. These quantities are expressed in terms of the stiffness and compliance tensors, respectively, but as noted above these are simply matrix inverses of one another. The Reuss bound should always be less than or equal to the Voigt bound and is the one that should be compared to bulk modulus values obtained from EOS fits to hydrostatic compression data. Values of the calculated isotropic moduli are included in Table IV. The results for the polarizable and nonpolarizable FFs are quite similar. For the polarizable FF we obtained $K_{Reuss}^{pol} = 14$ GPa, $G_{Reuss}^{pol} = 2.0$ GPa, and for the nonpolarizable one $K_{Reuss}^{nonpol} = 13.2$ GPa and $G_{Reuss}^{nonpol} = 1.8$ GPa. These numbers overlap to within the estimated uncertainties. The Voigt average bulk and shear moduli are factors of 1.6 and 6.3 times larger than the corresponding Reuss average values. These large differences for the two bounds are indicative of the large anisotropy of the crystal.

The atmospheric pressure isothermal bulk modulus can also be determined from an EOS fit to unit cell volume versus pressure data along the 300 K isotherm. For this purpose we fit V•P• at 300 K with a third-order Birch–Murnaghan EOS[45,46] performed in the P-V/V_0 plane with uniform weighting of the simulated data points. In Table V we pro-

TABLE V. Isothermal bulk modulus K_{B-M} and initial pressure derivative K'_{B-M} obtained from fits to third-order Birch–Murnaghan EOS.

	Simulation polarizable FF	Simulation nonpolarizable FF	Experiment Stevens et al. •Ref. 13•[a]	Experiment Olinger et al. •Ref. 12•[b]
K_{B-M} •GPA•	14.8	11.7	13.6• 0.6	16.7
K'_{B-M}	8.7	11.9	12.4• 1.1	S.7

[a]Below 8 GPa.
[b]Parameters originally reported in Ref. 13.

vide the corresponding isothermal bulk moduli and initial pressure derivatives $K• = dK/dP$. The predicted values are $K_{BM}^{pol} = 14.8$ GPa and $K_{BM}^{nonpol} = 11.7$ GPa for the initial bulk moduli for the polarizable and nonpolarizable FFs, respectively, and $K_{BM}^{pol} = 8.7$ and $K•_{BM}^{nonpol} = 11.9$ for the corresponding initial pressure derivatives. The EOS-based prediction of bulk modulus for the polarizable FF falls within the • 1• standard error envelope for the Reuss average value obtained directly from the elastic compliance tensor, whereas for the nonpolarizable FF the EOS-based value is • 3• below the Reuss average one.

We also include in Table V the bulk modulus values extracted from the experimental room-temperature isotherms of Stevens et al.[13] and Olinger et al.[12] by fitting to the third-order Birch–Murnaghan EOS. In their paper Stevens et al.[13] included fits for three different EOSs—Murnaghan, Vinet, and third-order Birch–Murnaghan—and also results reported by or derived from earlier theoretical studies due to Pastine and Bernecker[16] and Byrd et al.;[17] we have not included the two theoretical values in the present study. Stevens et al.[13] obtained values $K_{B-M} = 13.6$ GPa for the fit to their own data •restricted to pressures below 8 GPa• and $K_{B-M} = 16.7$ GPa for their fit to the isotherm of Olinger et al.[12] which extended up to P = 7.47 GPa.

Temperature dependence of stiffness coefficients. In Fig. 7 we show for both FFs the predicted temperature dependence of the nine "orthotropic" stiffness coefficients for compression C_{11}, C_{22}, C_{33} •panel a•, shear C_{44}, C_{55}, C_{66} •panel b•, and dilation C_{12}, C_{13}, and C_{23} •panel c•. The results for the two FFs are similar and qualitatively reasonable. It is seen in panel a that the compressive elements all undergo thermal softening, with the larger coefficients C_{11} and C_{22} undergoing larger net decreases than C_{33} over the 200 K temperature interval studied. The shear elements C_{44} and C_{55} are nearly independent of temperature for both FFs, whereas C_{66} decreases by several GPa; starting from values that differ by • 3 GPa at 200 K, the decrease in C_{66} is greater for the polarizable FF than for the nonpolarizable one such that the two values are comparable at 400 K. All three dilational stiffness coefficients C_{12}, C_{13}, and C_{23} decrease with increasing temperature; we find decreases of • one GPa for C_{13} and C_{23}, while C_{12} decreases by • 5 GPa over the same temperature interval.

Pressure dependence of the stiffness coefficients. The pressure dependence of selected stiffness coefficients at 300 K is shown for both FFs in Fig. 8. The changes with pressure between zero and 10 GPa are significantly greater than was the case for temperature dependence over the 200 K
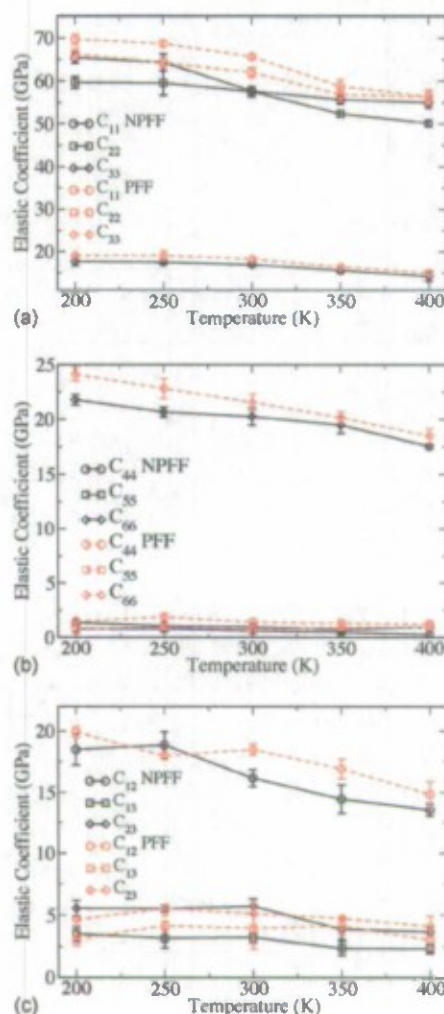

FIG. 7. Temperature dependence of selected stiffness coefficients for TATB crystal at P = 0 GPa for the polarizable and nonpolarizable FFs •dashed and solid connecting lines, respectively•. Panel a: compression coefficients C_{11}, C_{22}, and C_{33}. Panel b: shear coefficients C_{44}, C_{55}, and C_{66}. Panel c: dilational coefficients C_{12}, C_{13}, and C_{23}. Uncertainties represent one estimated standard deviation of the mean.

interval studied. With an important exception noted below, the results are in accord with expectations based on the discussion of the general form of the elastic tensor for TATB crystal. For example, C_{11} and C_{22} both increase from • 60 to • 250 GPa under compression, whereas C_{33} increases from • 20 GPa up to only • 100 GPa; and the increase in C_{66} is much larger than the increase in C_{44} and C_{55} which remain below 5 GPa for all pressures. A large anisotropy is also noted for the dilational coefficients, with a much larger increase in C_{12} than for C_{13} or C_{23}.

We note that the polarizable FF yields seemingly anomalous results for pressures above 6 GPa; seven of the nine stiffness coefficients shown in Fig. 8 soften considerably for P• 8 GPa, in some cases to values less than those obtained at 6 GPa. For instance, at P = 6 GPa, C_{11}• 200 GPa for both FFs; at P = 10 GPa, C_{11} for the nonpolarizable FF has increased to • 250 GPa •following a smooth, monotonic trend curve• while for the polarizable one C_{11} has remained approximately constant over that 4 GPa pressure interval. •In
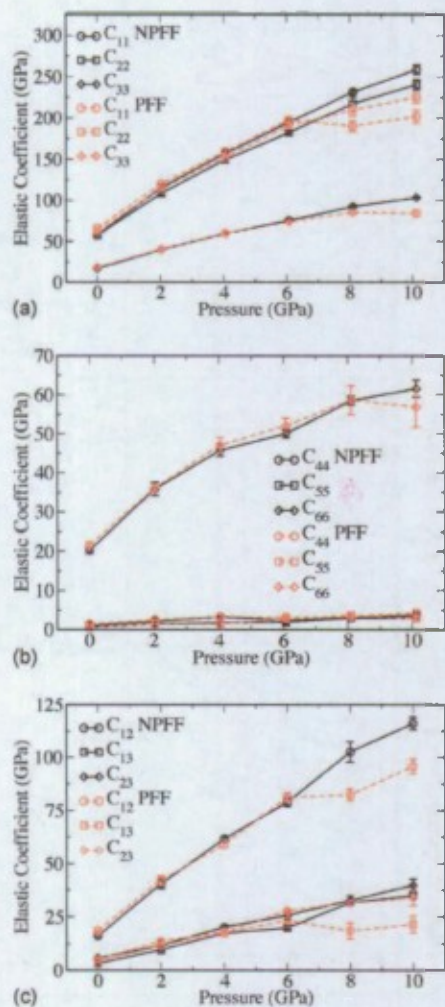
FIG. 8. As in Fig. 7 except that the pressure dependence of selected stiffness coefficients is shown for T=300 K.

FIG. 9. Temperature dependence at P=0 GPa •panel a• and pressure dependence at T=300 K •panel b• of the Reuss average isotropic moduli for TATB crystal for the polarizable and nonpolarizable FFs •dashed and solid connecting lines, respectively•. Uncertainties represent one estimated standard deviation of the mean.

some cases the change in behavior occurs between 6 and 8 GPa while in others it occurs between 8 and 10 GPa.• Since there is no evidence for a phase transition in the lattice parameters and unit cell volumes on the 300 K isotherm shown in Figs. 3–5, this behavior for the stiffness coefficients seems to be unphysical. We note that in previous work for PETN in which a similar polarizable FF development protocol was applied, a structural phase transition was observed at P• 7 GPa when using the polarizable FF developed there; whereas there was no evidence for one based on the nonpolarizable FF model. At such high pressures intermolecular separations between heavy atoms •carbons, nitrogens, and oxygens• are often less than 2.7 Å. It turns out that for such short separations the selected Thole screening functional with $a_T = 0.2$ is not strong enough to sufficiently damp interactions between induced dipoles, which leads to unrealistically weaker repulsive interactions between these atoms and therefore results in softer stiffness coefficients obtained from simulations. We found that reduction in a_T to 0.1, in principle, eliminates this artifact and simulations with polarizable FF predict elastic constants that follow a trend similar to those obtained using nonpolarizable FF for pressures above 6 GPa. However, while this empirical adjustment ap-
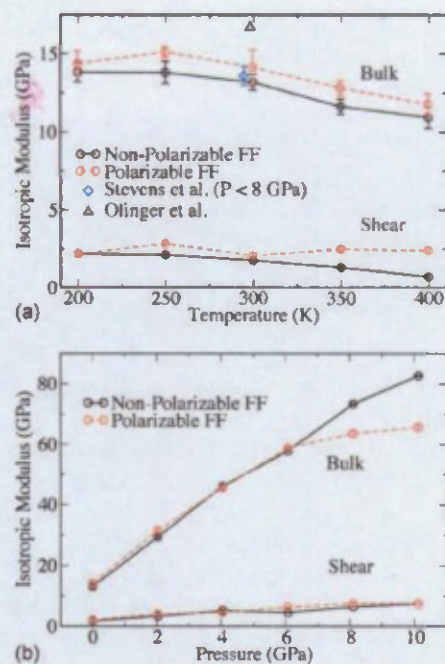
pears to provide reasonable predictions, $a_T = 0.1$ in the selected Thole screening functional form results in an unrealistically large screening length for the induced-dipole/induced-dipole interaction. We believe that perhaps use of other functional forms with more realistic values for the screening length[47] or implementation of Gaussian distributed •instead of point• charges and dipoles would likely resolve this apparent roadblock for reliable use of polarizable FF for simulations at high pressures. We recommend that applications of the polarizable FF with current treatment of induced polarization be restricted to pressures of 6 GPa or less.

Temperature and pressure dependence of isotropic bulk and shear moduli. Finally, we present in Fig. 9 the temperature dependence •panel a• and pressure dependence •panel b• of the Reuss average isotropic moduli for both FFs. With the exception noted above for the polarizable FF at high pressure, the results for the two FFs are similar. The bulk modulus for both FFs exhibits modest decreases with temperature •panel a•. The shear modulus for the nonpolarizable FF decreases from • 2.4 to • 1 GPa between 200 and 400 K, whereas for the polarizable FF the shear modulus is essentially independent of temperature •panel a•. Under compression, the bulk modulus for the nonpolarizable FF increases from • 14 to • 82 GPa, whereas the shear modulus increases only from • 2 to • 4 GPa •panel b•. The behavior of the stiffness tensor noted for the polarizable FF in Fig. 8 results in increased negative curvature in the bulk modulus for P• 6 GPa but little if any discernable effect on the shear modulus compared to the result for the nonpolarizable FF.

IV. CONCLUSIONS

Atomistic simulations of TATB crystal have been conducted using polarizable and nonpolarizable FFs. We found

that inclusion of induced polarization effects is essential in providing simultaneously accurate descriptions of crystal structure and heat of sublimation of TATB crystal. However, it appears that these effects can be effectively taken into account in the nonpolarizable FF by increasing partial atomic charges by 20% relative to values in the polarizable form. The latter approach is about a factor of two more computationally efficient at normal pressure and a factor of 2.6 more efficient at high pressure •10 GPa• compared to the polarizable model. Predicted pressure dependencies of unit cell dimensions are in very good agreement with experimental data in the entire pressure range up to 10 GPa. Heat of sublimation and temperature dependence of unit cell dimensions obtained from simulations were also found to be in good agreement with experiment. This agreement with experimental data provides us confidence that simulation predicted elastic coefficients of TATB crystal and reported here for the first time are reliable. Analysis of stiffness coefficients showed larger anisotropy of elastic, shear, and dilation components consistent with the sheet stacking motif of TATB crystal.

ACKNOWLEDGMENTS

[1] J. R. Travis, "TATB: The IHE exemplar," Report No. LA-UR-92-3883, 1992.

[2] B. M. Dobratz, "The insensitive high explosive triaminotrinitrobenzene •TATB•: Development and characterization—1888 to 1994," Report No. LA-13014-H, 1995.

[3] K. K. Baldridge and J. S. Siegel, J. Am. Chem. Soc. **115**, 10782 •1993•.

[4] C. Y. Zhang, Chem. Phys. **324**, 547 •2006•.

[5] G. Filippini and A. Gavezzotti, Chem. Phys. Lett. **231**, 86 •1994•.

[6] D. S. Phillips, R. B. Schwarz, C. B. Skidmore, M. A. Hiskey, and S. F. Son, AIP Conf. Proc. **505**, 707 •2000•.

[7] J. E. Kennedy, K.-Y. Lee, S. F. Son, E. S. Martin, B. W. Asay, C. B. Skidmore, AIP Conf. Proc. **505**, 711 •2000•.

[8] S. F. Son, B. W. Asay, B. F. Henson, R. K. Sander, A. N. Ali, P. M. Zielinski, D. S. Phillips, R. B. Schwarz, and C. B. Skidmore, J. Phys. Chem. B **103**, 5434 •1999•.

[9] C. Zhang, J. Phys. Chem. B **111**, 14295 •2007•.

[10] H. H. Cady and A. C. Larson, Acta Crystallogr. **18**, 485 •1965•.

[11] J. R. Kolb and H. F. Rizzo, Propellants, Explos., Pyrotech. **4**, 10 •1979•.

[12] B. Dlinger and H. H. Cady, Proceedings of the Sixth International Detonation Symposium, 1976 •unpublished•, p. 700.

[13] L. L. Stevens, N. Valisavljevic, D. E. Hooks, and D. M. Dattelbaum, Propellants, Explos., Pyrotech. **33**, 286 •2008•.

[14] M. Pravica, B. Yulga, Z. X. Liu, and D. Tschauner, Phys. Rev. B **76**, 064102 •2007•.

[15] M. Pravica, B. Yulga, S. Tkachev, and Z. X. Liu, J. Phys. Chem. A **113**, 9133 •2009•.

[16] D. J. Pastine and R. R. Bernecker, J. Appl. Phys. **45**, 4458 •1974•.

[17] E. F. C. Byrd and B. M. Rice, J. Phys. Chem. **111**, 2787 •2007•.

[18] T. D. Sewell, Mater. Res. Soc. Symp. Proc. **418**, 67 •1996•.

[19] R. H. Gee, S. Roszak, K. Balasubramanian, and L. E. Fried, J. Chem. Phys. **120**, 7059 •2004•.

[20] W. L. Jorgensen, D. S. Maxwell, and J. Tirado-Rives, J. Am. Chem. Soc. **118**, 11225 •1996•.

[21] J. M. Wang, R. M. Wolf, J. W. Caldwell, P. A. Kollman, and D. A. Case, J. Comput. Chem. **25**, 1157 •2004•.

[22] N. Rai, D. Bhatt, J. I. Siepmann, and L. E. Fried, J. Chem. Phys. **129**, 194510 •2008•.

[23] R. G. Garza, LLNL Report No. UCRL-82723, 1979.

[24] J. M. Rosen and C. Dickinson, J. Chem. Eng. Data **14**, 120 •1969•.

[25] A. T. Hagler, S. Lifson, and P. Dauber, J. Am. Chem. Soc. **101**, 5122 •1979•.

[26] J. A. Maple, M.-J. Hwang, T. P. Stockfisch, U. Dinur, M. Waldmn, C. S. Ewig, and A. T. Hagle, J. Comput. Chem. **15**, 162 •1994•.

[27] H. Sun, J. Phys. Chem. **102**, 7338 •1998•.

[28] S. L. Mayo, B. D. Dlafson, and W. A. Goddard III, J. Phys. Chem. **94**, 8897 •1990•.

[29] A. K. Rappe, C. J. Casewit, K. S. Colwell, W. A. Goddard III, and W. M. Skiff, J. Am. Chem. Soc. **114**, 10024 •1992•.

[30] R. H. Gee, A. Maiti, S. Bastea, and L. E. Fried, Macromolecules **40**, 3422 •2007•.

[31] D. Borodin, J. Phys. Chem. B **113**, 11463 •2009•.

[32] D. Borodin, G. D. Smith, T. D. Sewell, and D. Bedrov, J. Phys. Chem. B **112**, 734 •2008•.

[33] B. T. Thole, Chem. Phys. **59**, 341 •1981•.

[34] D. Borodin and G. D. Smith, J. Phys. Chem. B **110**, 6279 •2006•.

[35] M. Waldman and A. T. Hagler, J. Comput. Chem. **14**, 1077 •1993•.

[36] M. J. Frisch et al., GAUSSIAN98, Revision A.7, Gaussian, Inc., Pittsburgh, PA, 1998.

[37] See EPAPS supplementary material at http://dx.doi.org/10.1063/1.3264972 for additional data on force field parameterization and simulation predicted compliance tensor and elastic coefficients.

[38] G. D. Smith, R. K. Bharadwaj, D. Bedrov, and C. Ayyagari, J. Chem. Phys. B **103**, 705 •1999•.

[39] http://www.eng.utah.edu/~gdsmith/lucretius.html

[40] B. J. Palmer, J. Comput. Phys. **104**, 470 •1993•.

[41] T. D. Sewell, R. Menikoff, D. Bedrov, and G. D. Smith, J. Chem. Phys. **119**, 7417 •2003•.

[42] G. J. Martyna, M. E. Tuckerman, D. J. Tobias, and M. L. Klein, Mol. Phys. **87**, 1117 •1996•.

[43] The one exception to this is the case $T = 200$ K at atmospheric pressure, for which the error bars after 1.0 ns of simulation production were considerably larger than for the other cases considered at atmospheric pressure. For this reason, 2.0 ns of production simulation was performed for that case, and the error bar estimates for the elastic stiffness and compliance tensors were obtained from four 500 ps subaverages rather than 250 ps ones.

[44] M. Parrinello and A. Rahman, J. Chem. Phys. **76**, 2662 •1982•.

[45] J.-P. Poirier, Introduction to the Physics of the Earth's Interior •Cambridge University, Cambridge, 1999•, p. 64.

[46] R. Menikoff and T. D. Sewell, High Press. Res. **21**, 121 •2001•.

[47] P. Cieplak, F.-Y. Dupradeau, Y. Duan, and J. Wang, J. Phys.: Condens. Matter **21**, 333102 •2009•.